Eur. Phys. J. Special Topics **224**, 2703–2717 (2015)
© EDP Sciences, Springer-Verlag 2015
DOI: 10.1140/epjst/e2015-02584-6

THE EUROPEAN PHYSICAL JOURNAL SPECIAL TOPICS

Regular Article

Adaptive tuned piezoelectric MEMS vibration energy harvester using an electrostatic device

H. Madinei, H. Haddad Khodaparast, S. Adhikari, M.I. Friswell, and M. Fazeli

College of Engineering, Swansea University, Singleton Park, Swansea SA2 8PP, UK

Received 21 August 2015 / Received in final form 9 September 2015
Published online 20 November 2015

Abstract. In this paper an adaptive tuned piezoelectric vibration based energy harvesting system based on the use of electrostatic device is proposed. The main motivation is to control the resonance frequency of the piezoelectric harvester with the DC voltage applied to the electrostatic system in order to maximize the harvested power. The idea is demonstrated in a hybrid system consisting of a cantilevered piezoelectric harvester combined with an electrostatic harvester which is connected to a variable voltage source. The nonlinear governing differential equation of motion is derived based on Euler Bernoulli theory, and solved to obtain the static and dynamic solutions. The results show that the harvester can be tuned to give a resonant response over a wide range of frequencies, and shows the great potential of this hybrid system.

1 Introduction

With the advances made in small scale fabrication, Micro Electro Mechanical Systems (MEMS) have gained growing attention over recent years [1,2]. These devices need low power, in the range of microwatts. In many applications, the harvesting of ambient energy has been recognized as an important source of power for micro structures [3]. There are various types of ambient sources such as light, heat and mechanical vibration which can be used to scavenge energy. Among these, mechanical vibration has been demonstrated to offer great potential since there is much wasted mechanical energy in our environment. This ambient source of energy can be converted to useful electrical energy by a range of electromechanical converters [4,5]. The most common types of transduction methods are electromagnetic [6], piezoelectric [7] and electrostatic [8]; piezoelectric and electrostatic approaches are the most common and practical in MEMS scale harvesters. Fabrication requirements of magnetic MEMS harvesters, such as high processing temperatures which are not compatible with the Complementary Metal–Oxide–Semiconductor (CMOS) process, makes integrating high performance magnets in MEMS devices harvesters very difficult [9].

So far, there have been several researches on the piezoelectric based harvesters at micro scales. Jeon et al. [10] studied a $170\,\mu\text{m} \times 260\,\mu\text{m}$ PZT beam power generator that can harvest $1\,\mu$W power output across a 5.2 MΩ resistive load from a 10.8 g vibration at its resonant frequency of 13.9 kHz. Subsequently, a second generation of Piezoelectric Micro Power Generator (PMPG) was proposed by the same group [11].

They considered the effect of proof mass, beam shape and damping on the performance of the system and showed that the maximum harvested power occurs when the resonant frequency of the energy harvester matches the dominant excitation frequency. Feng et al. [12] investigated a MEMS based PZT cantilever power generator with a proof mass and showed that the system is capable of harvesting 2.16 μW from a 1g vibration at its resonant frequency of 609 Hz. While the demonstrated power density is quite high, the proof mass was not integrated with the cantilever beam. There is difficulty in fabricating high quality PZT thin films and/or the complex process procedures to produce MEMS PZT-based cantilever with an integrated proof mass at the end tip. A PZT-based micro cantilever with an integrated proof mass was not manufactured until 2007. Renaud et al. [13,14] reported the fabrication, modeling, and characterization of a MEMS piezoelectric cantilever power generator with an integrated proof mass that can generate an average power of 40 μW at 1.8 kHz. Shen et al. [15] designed a MEMS piezoelectric energy harvesting device for low vibration frequency and high vibration amplitude environment. They showed that with a beam dimension of 4.8 mm $\times$ 0.4 mm $\times$ 0.036 mm, 2.15 μW power can be harvested at 461.15 Hz. Gu et al. [16,17] proposed an impact-driven FUC (Frequency Up-conversion Mechanisms) energy harvesting prototype that is illustrated to be suitable for MEMS implementation. In this model, the ambient low frequency is up-converted to high resonant frequency by the periodic impact between the driving beam and two rigid generating beams. Another advantage of a vibro-impacting system is the capability of improving output power [18].

Electrostatic harvesters are another type of harvester and the energy conversion capability of these harvesters tends to be higher at the MEMS scale. These harvesters can be fabricated in a silicon micromachined process which is compatible with CMOS. They scavenge energy based on the electrostatic force of a variable capacitor and work under constant charge or voltage conditions. Generally, operating harvesters in voltage constrained cycles provide more energy compared to a charge constrained cycle [19]. In capacitive harvesters, due to the mechanical vibration, the gap distance or/and overlap area of the electrodes of the variable capacitance change and this produces the electrical energy. To ensure the conversion cycle in these convertors, the charging of the capacitor at all times is required and this can be achieved using electret based or electret free approaches [20,21]. However, electret based harvesters have power densities inferior to those employing variable capacitors [22].

Many electrostatic harvesters have been developed by several authors at small scales. Meninger et al. [23] studied an energy harvester and obtained 8 μW at 2.52 kHz from an in-plane overlap electrostatic generator. Ma et al. [24] proposed an electrostatic generator and achieved 0.065 μW from a 4.5 kHz vibration. Kuehne et al. [25] reported a resonant based electrostatic MEMS device with an out-of-plane gap closing mechanism which provided an output power of 4.28 μW under vibration with frequency 1 kHz and amplitude 1.96 m/s^2, i.e. 0.2 g. Chiu et al. [26] developed an electrostatic MEMS energy harvester using an in-plane gap closing mechanism with a 1 cm^2 chip area. An AC output power of 1.2 μW with a load of 5 MΩ was measured at 1.87 kHz. In general, the electrostatic mechanism has the lowest energy harvesting capabilities amongst the other types of energy harvesters [27]. However electrostatic energy harvesters do have specific advantages and areas of application. For example, they are mainly made of silicon by using semiconductor fabrication technology and this facilitates CMOS integration.

An important requirement in the field of MEMS scale energy harvesters is to widen the operating frequency band and consequently maximize the energy harvested from the device. Petropoulos et al. [28] used coupled oscillators with two springs, two masses and two dampers and showed that this system has a flat response for power generation over a wider frequency range. Feng et al. [29] proposed a micromechanical

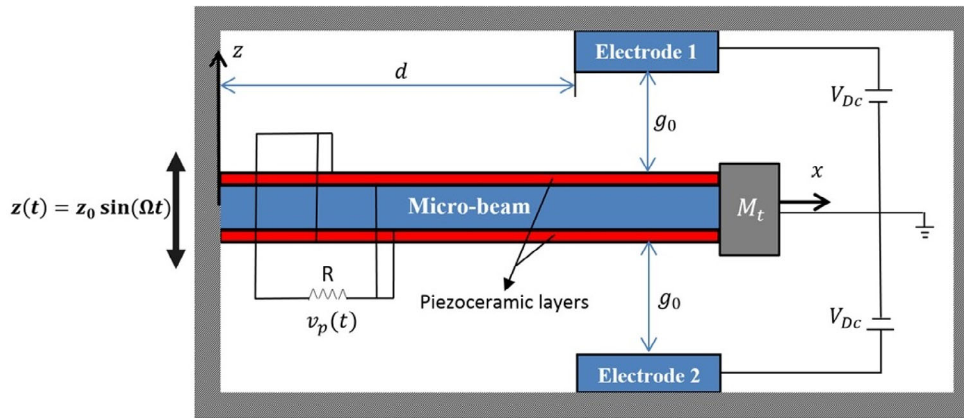

Fig. 1. Schematic of the proposed energy harvester.

piezoelectric energy harvesting device which consisted of four parallel cantilever beams with different natural frequencies. The presence of four beams with different natural frequencies increases the range of operational frequency of their system. Wu et al. [30] proposed a piezoelectric energy harvester with a moveable proof mass that could adjust the natural frequency of the harvester system and therefore widen the range of operational frequency. Most of the studies on adjustable MEMS energy harvesting systems has focused on the use of additional mass or/and stiffness-damping elements. To our knowledge, there are no other studies in the hybrid use of electrostatic and piezoelectric MEMS harvesters in which the electrostatic device is used to increase the range of operational frequencies.

This paper presents a new type of hybrid MEMS harvester which employs electrostatic and piezoelectric harvesting mechanisms. The maximum power is harvested when the system is excited at its resonance frequency. However, in real applications the environmental excitation frequency will often change and not always be identical to the resonant frequency. Since the harvester system needs to operate over a wide range of frequencies, for efficient operation a frequency tuning mechanism is required. In this paper, the electrostatic device is used as a frequency tuning device, where the resonance frequency of the system is changed by varying the DC voltage applied to the electrostatic device. This is performed conveniently via a variable voltage source, and therefore the natural frequency of the harvester system is tuned to the environmental excitation frequency. The proposed energy harvester is a micro-cantilever electrode beam with two layers of piezoelectric material bonded on the top and bottom surfaces of the beam and two electrodes located at a fixed distance from the top and bottom of the beam tip.

2 Model description and mathematical modelling

Figure 1 shows the model used in this paper. The model is an isotropic micro-beam of length L, width a, thickness h, density ρ and Young's modulus E, sandwiched with piezoceramic layers having thickness h_0, Young's modulus E_0 and density ρ_0 throughout the micro-beam length and located between two electrodes (electrode 1 and electrode 2). The coordinate system, as illustrated in Fig. 1, is attached to the middle of the left end of the micro-beam where x and z refer to the horizontal and vertical coordinates respectively. The tip mass (or proof mass) M_t is attached to the

cantilever beam in order to decrease its natural frequency. The tip mass is used to control the dynamics of the micro-cantilever. When the tip mass is much larger than the mass of the cantilever beam, a simple SDOF model can be used to model the harvester. The governing equation of transverse motion can be written as [31,32]

$$(EI)_{eq}\frac{\partial^4 w(x,t)}{\partial x^4}+(\rho A)_{eq}\frac{\partial^2 w(x,t)}{\partial t^2}+c_a\frac{\partial w(x,t)}{\partial t}-\vartheta v(t)\left(\frac{d\delta(x)}{dx}-\frac{d\delta(x-L)}{dx}\right)$$
$$=\frac{\varepsilon_0 a H(x-d)}{2}\left(\frac{V_{DC}^2}{(g_0-w)^2}-\frac{V_{DC}^2}{(g_0+w)^2}\right)-\left((\rho A)_{eq}+M_t\delta(x-L)\right)\frac{\partial^2 z(t)}{\partial t^2}, \tag{1}$$

where

$$(EI)_{eq}=\frac{2a}{3}\left(E\frac{h^3}{8}+E_0\left(\left(h_0+\frac{h}{2}\right)^3-\frac{h^3}{8}\right)\right),\quad (\rho A)_{eq}=a(\rho h+2\rho_0 h_0),$$

and subjected to the following boundary conditions:

$$w(0,t)=0,\quad \frac{\partial w(0,t)}{\partial x}=0,$$
$$\frac{\partial}{\partial x}\left((EI)_{eq}\frac{\partial^2 w(L,t)}{\partial x^2}\right)=M_t\left(\frac{\partial^2 w(L,t)}{\partial t^2}\right),$$
$$(EI)_{eq}\frac{\partial^2 w(L,t)}{\partial x^2}=-I_{M_t}\frac{\partial^2}{\partial t^2}\left(\frac{\partial w(L,t)}{\partial x}\right). \tag{2}$$

In Eq. (1), $w(x,t)$ is the transverse deflection of the beam relative to its base at the position x and time t, c_a is the viscous air damping coefficient, ε_0 is the permittivity of free space, $H(x)$ is the Heaveside function, $\delta(x)$ is the Dirac delta function, V_{DC} is the applied DC voltage to micro-beam, g_0 is the air gap between electrodes (the system is assumed to be symmetric), $z(t)$ is the base excitation function, $v(t)$ is the voltage across the electrodes of each piezoceramic layer and ϑ is the backward coupling term which is dependent on the type of connection between the piezoceramic layers (i.e. series or parallel connections). In series, the two piezoelectric layers are oppositely polarized and produce a larger voltage output; whereas in parallel, the two piezoelectric layers are polarized in the same direction, and a larger current output is achievable. For the series and parallel connection cases the backward coupling term can be respectively expressed as [31]

$$\vartheta_s=\frac{\bar{e}_{31}a}{2h_0}\left(\left(h_0+\frac{h}{2}\right)^2-\frac{h^2}{4}\right),\vartheta_p=2\vartheta_s=\frac{\bar{e}_{31}a}{h_0}\left(\left(h_0+\frac{h}{2}\right)^2-\frac{h^2}{4}\right), \tag{3}$$

where subscripts s and p denote series and parallel connections of the piezoceramic layers and $\bar{e}_{31}$ is the equivalent piezoelectric coefficient. By considering parallel connection between these layers (see Fig. 1) and $z_0\sin(\Omega t)$ as a base excitation,

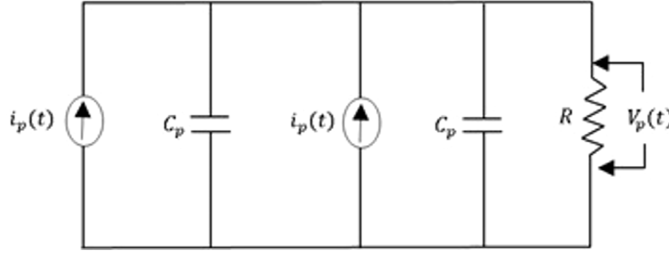

Fig. 2. Electrical circuit showing the parallel connection of the piezoceramic layers.

Eq. (1) can be written as

$$(EI)_{eq}\frac{\partial^4 w\left(x,t\right)}{\partial x^4}+(\rho A)_{eq}\frac{\partial^2 w\left(x,t\right)}{\partial t^2}+c_a\frac{\partial w\left(x,t\right)}{\partial t}-\vartheta_p v_p\left(t\right)\left(\frac{d\delta\left(x\right)}{dx}-\frac{d\delta\left(x-L\right)}{dx}\right)$$
$$=\frac{\varepsilon_0 aH\left(x-d\right)}{2}\left(\frac{V_{DC}^2}{\left(g_0-w\right)^2}-\frac{V_{DC}^2}{\left(g_0+w\right)^2}\right)+z_0\Omega^2\left((\rho A)_{eq}+M_t\delta\left(x-L\right)\right)\sin\left(\Omega t\right), \tag{4}$$

and the electrical circuit equation (see Fig. 2) based on Kirchhoff's laws can be expressed as

$$C_p\frac{dv_p\left(t\right)}{dt}+\frac{v_p\left(t\right)}{2R}-i_p\left(t\right)=0, \tag{5}$$

where the internal capacitance (C_p) and the current source can be obtained as [30]

$$C_p=\frac{\bar{\varepsilon}_{33}^s aL}{h_0},\quad i_p(t)=-\frac{\bar{e}_{31}a}{2}(h_0+h)\int_0^L\frac{\partial^3 w(x,t)}{\partial x^2\partial t}dx. \tag{6}$$

and $\bar{\varepsilon}_{33}^s$ is the permittivity component at constant strain with the plane stress assumption for the beam.

There is a second electrical circuit, which is related to the electrostatic part of the model, as shown in Fig. 3. The main components are two variable capacitors (C_{v1} and C_{v2}) which are formed by the out-of-plane gap closing of the electrodes, where one plate or electrode is fixed and the other is movable. There are four diodes which help to store the harvested charge in the storage capacitor (C_T). As shown in Fig. 1, the microbeam is the moveable part of the variable capacitances and electrodes 1 and 2 are considered as fixed. The variable capacitors are charged by an external voltage source (V_{DC}) and their capacitances can be expressed as

$$C_{v1}=\frac{\varepsilon_0 A_e}{\left(g_0+w_{\mathrm{av}}\right)},\quad C_{v2}=\frac{\varepsilon_0 A_e}{\left(g_0-w_{\mathrm{av}}\right)} \tag{7}$$

where A_e is the overlapping area between the fixed and moveable electrodes and w_{av} is the average value of w in this area. The conversion cycle starts when the variable capacitors are charged to the maximum voltage, and then due to the mechanical movement, the capacitance of the variable capacitor changes and since the voltage is constant, a current is generated which can be stored in the storage capacitance (C_T).

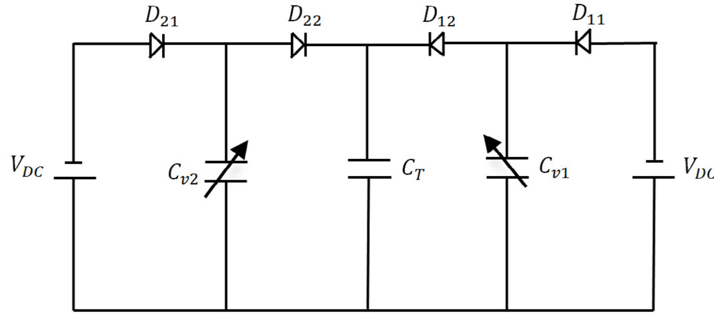

Fig. 3. Electrical circuit showing the electrostatic part of the harvester.

3 Problem solution

3.1 Static analysis

Above a certain applied DC voltage electrostatic MEMS devices can become statically unstable. This voltage is known as the pull-in voltage, and may be obtained from the static solution of Eqs. (4) and (5). If the time varying terms in these equations are set to zero, then the equation corresponding to the static deflection is

$$(EI)_{eq}\frac{d^4 w_s(x)}{dx^4} = \frac{\varepsilon_0 a H(x-d)}{2}\left(\frac{V_{DC}^2}{(g_0-w_s)^2} - \frac{V_{DC}^2}{(g_0+w_s)^2}\right). \tag{8}$$

Due to the nonlinearity of the electrostatic force, the solution is complicated and time consuming. Directly applying the Galerkin method [33] or the finite difference method creates a set of non-linear algebraic equations. In this paper, a two-step incremental method is used to solve the governing nonlinear algebraic equations. First, the step by step linearization method (SSLM) [34] is applied and second, the Galerkin method is used to solve the resulting linear equations. To use the SSLM, suppose that w_s^k is the displacement of the beam due to an applied DC voltage(V_{DC}). Increasing the applied voltage to a new value, gives the displacement

$$w_s^{k+1} = w_s^k + \delta w_s = w_s^k + \psi(x), \tag{9}$$

when

$$V_{DC}^{k+1} = V_{DC}^k + \delta V. \tag{10}$$

Therefore, Eq. (8) at kth and $k+1$th steps can be rewritten as

$$(EI)_{eq}\frac{d^4 w_s^k(x)}{dx^4} = \frac{\varepsilon_0 a H(x-d)}{2}\left(\frac{\left(V_{DC}^k\right)^2}{\left(g_0-w_s^k\right)^2} - \frac{\left(V_{DC}^k\right)^2}{\left(g_0+w_s^k\right)^2}\right), \tag{11a}$$

$$(EI)_{eq}\frac{d^4 w_s^{k+1}(x)}{dx^4} = \frac{\varepsilon_0 a H(x-d)}{2}\left(\frac{\left(V_{DC}^{k+1}\right)^2}{\left(g_0-w_s^{k+1}\right)^2} - \frac{\left(V_{DC}^{k+1}\right)^2}{\left(g_0+w_s^{k+1}\right)^2}\right). \tag{11b}$$

Substituting Eq. (9) into Eq. (11b) gives

$$\begin{aligned}(EI)_{eq}&\frac{d^4 w_s^k(x)}{dx^4} + \frac{d^4\psi(x)}{dx^4}\\ &= \frac{\varepsilon_0 a H(x-d)}{2}\left(\frac{\left(V_{DC}^{k+1}\right)^2}{\left(g_0-w_s^k-\psi(x)\right)^2} - \frac{\left(V_{DC}^{k+1}\right)^2}{\left(g_0+w_s^k+\psi(x)\right)^2}\right).\end{aligned} \tag{12}$$

By considering a small value of δV, it is expected that $\psi(x)$ will also be small. Hence using of Calculus of Variations theory and the Taylor series expansion about w_s^k, the linearised coupled electrostatic forces are obtained, resulting in the equation for the beam displacement as

$$(EI)_{eq}\left(\frac{d^4 w_s^k(x)}{dx^4}+\frac{d^4\psi(x)}{dx^4}\right)=\frac{\varepsilon_0 aH(x-d)}{2}\left(\frac{\left(V_{DC}^{k+1}\right)^2}{\left(g_0-w_s^k\right)^2}-\frac{\left(V_{DC}^{k+1}\right)^2}{\left(g_0+w_s^k\right)^2}\right)$$
$$+\varepsilon_0 aH(x-d)\left(\frac{\left(V_{DC}^{k+1}\right)^2}{\left(g_0-w_s^k\right)^3}+\frac{\left(V_{DC}^{k+1}\right)^2}{\left(g_0+w_s^k\right)^3}\right)\psi(x). \tag{13}$$

Substituting for $\frac{d^4 w_s^k(x)}{dx^4}$ from Eq. (11a) into Eq. (13) gives

$$L(\psi)=(EI)_{eq}\frac{d^4\psi}{dx^4}-\varepsilon_0 aH(x-d)\left(\frac{\left(V_{DC}^{k+1}\right)^2}{\left(g_0-w_s^k\right)^3}+\frac{\left(V_{DC}^{k+1}\right)^2}{\left(g_0+w_s^k\right)^3}\right)\psi(x)$$
$$-\frac{\varepsilon_0 aH(x-d)}{2}\left(\frac{\left(V_{DC}^{k+1}\right)^2-\left(V_{DC}^{k}\right)^2}{\left(g_0-w_s^k\right)^2}-\frac{\left(V_{DC}^{k+1}\right)^2-\left(V_{DC}^{k}\right)^2}{\left(g_0+w_s^k\right)^2}\right)=0. \tag{14}$$

This linear differential equation is now solved by the Galerkin method. $\psi(x)$ is approximated by

$$\psi(x)=\sum_{i=1}^{N} s_i\varphi_i(x). \tag{15}$$

The approximate solution is constructed by expressing the $\psi(x)$ as a linear combination of a complete set of linearly independent shape functions $\varphi_i(x)$ multiplied by weights s_i. The functions $\varphi_i(x)$ satisfy the boundary conditions. Substituting Eq. (15) into Eq. (14), and multiplying by $\varphi_j(x)$ as a weight function in the Galerkin method and integrating from $x=0$ to L, gives a set of linear algebraic equations as

$$\sum_{j=1}^{N} K_{ij}s_j=F_j,\ i=1,\ldots,N \tag{16a}$$

$$K_{ij}=K_{ij}^{mech}-K_{ij}^{elec}, \tag{16b}$$

where

$$K_{ij}^{mech}=(EI)_{eq}\int_0^L \varphi_i^{IV}(x)\varphi_j(x)\,dx,$$
$$K_{ij}^{elec}=\varepsilon_0 a\left(V_{DC}^{k+1}\right)^2\int_0^L\left(\frac{H(x-d)}{\left(g_0-w_s^k\right)^3}+\frac{H(x-d)}{\left(g_0+w_s^k\right)^3}\right)\varphi_i(x)\varphi_j(x)\,dx,$$
$$F_j=\frac{\varepsilon_0 a\left(\left(V_{DC}^{k+1}\right)^2-\left(V_{DC}^{k}\right)^2\right)}{2}\int_0^L\left(\frac{H(x-d)}{\left(g_0-w_s^k\right)^2}-\frac{H(x-d)}{\left(g_0+w_s^k\right)^2}\right)\varphi_j(x)\,dx. \tag{17}$$

As it can be seen in Eqs. (16b) and (17), the electrical stiffness creates a negative stiffness which opposes the mechanical stiffness. At the pull-in voltage the lowest eigenvalue of K_{ij} becomes zero.

3.2 Dynamic analysis

The dynamic behaviour of the system is studied using the Galerkin based reduced order method [33]. As mentioned previously, the direct application of the Galerkin method is time consuming due to the non-linearity of the electrostatic force. To overcome this difficulty, the electrostatic forcing terms in Eq. (4) is considered constant at each time step and takes the value of the previous step [35] (similar to the concept used for the static solution). By selecting sufficiently small time steps, this assumption leads to sufficiently accurate results. Then, Eq. (4) can be rewritten as

$$\begin{aligned}&(EI)_{eq}\frac{\partial^4 w\left(x,t\right)}{\partial x^4}+(\rho A)_{eq}\frac{\partial^2 w\left(x,t\right)}{\partial t^2}+c_a\frac{\partial w\left(x,t\right)}{\partial t}\\&-\vartheta_p v_p\left(t\right)\left(\frac{d\delta\left(x\right)}{dx}-\frac{d\delta\left(x-L\right)}{dx}\right)=\frac{\varepsilon_0 a V_{DC}^2}{2}\left(\frac{H\left(x-d\right)}{\left(g_0-\bar{w}\right)^2}-\frac{H\left(x-d\right)}{\left(g_0+\bar{w}\right)^2}\right)\\&+z_0\Omega^2\left((\rho A)_{eq}+M_t\delta\left(x-L\right)\right)\sin\left(\Omega t\right),\end{aligned}\tag{18}$$

where $\bar{w}$ is the micro-beam deflection obtained at the previous step (or initial condition at the first step), and w is the micro-beam deflection at the current step, which can be represented as a series expansion in terms of the eigenfunctions of the micro-beam, i.e.

$$w\left(x,t\right)=\sum_{i=1}^{N}U_i\left(t\right)\varphi_i\left(x\right),\tag{19}$$

where $\varphi_i\left(x\right)$ is the ith linear undamped mode shape of the straight micro-beam and $U_i\left(t\right)$ is the ith generalized coordinate. Equation (18) can be converted into a system of differential equations using the Galerkin method and written as

$$\begin{aligned}&(\rho A)_{eq}\sum_{i=1}^{N}\ddot{U}_i\int_0^L\varphi_i\left(x\right)\varphi_j\left(x\right)dx+c_a\sum_{i=1}^{N}\dot{U}_i\int_0^L\varphi_i(x)\varphi_j(x)dx\\&+(EI)_{eq}\sum_{i=1}^{N}U_i\int_0^L\varphi_i^{IV}\left(x\right)\varphi_j\left(x\right)dx-\vartheta_p v_p\left(t\right)\int_0^L\varphi_j\left(x\right)\left(\frac{d\delta\left(x\right)}{dx}-\frac{d\delta\left(x-L\right)}{dx}\right)dx\\&=\frac{\varepsilon_0 a V_{DC}^2}{2}\int_0^L\varphi_j\left(x\right)\left(\frac{H\left(x-d\right)}{\left(g_0-\bar{w}\right)^2}-\frac{H\left(x-d\right)}{\left(g_0+\bar{w}\right)^2}\right)dx\\&+z_0\Omega^2\left(\int_0^L\left((\rho A)_{eq}\varphi_j\left(x\right)+M_t\delta\left(x-L\right)\varphi_j\left(x\right)\right)dx\right)\sin\left(\Omega t\right),\end{aligned}\tag{20}$$

for $j=1,2,\ldots,N$, and

$$C_p\dot{\nu}_p+\frac{\nu_p}{2R}+\frac{\bar{e}_{31}a}{2}(h_0+h)\sum_{i=1}^{N}\dot{U}_i\int_0^L\varphi_i^{II}(x)dx=0.\tag{21}$$

Equations (20) and (21) represents a system of coupled nonlinear ordinary-differential equations describing the dynamic behavior of the micro-beam. A single-mode approximation yields the following equations

$$M\ddot{U}+C\dot{U}+KU-\theta_p\nu_p=F_e+F_b\sin(\Omega t),\tag{22}$$

$$p_2\dot{v}_p+p_3\nu_p=p_1\dot{U},\tag{23}$$

where

$$
\begin{aligned}
& M=(\rho A)_{eq}\int_0^L \varphi^2(x)\,dx, \quad C=c_a\int_0^L \varphi^2(x)\,dx,\\
& K=(EI)_{eq}\int_0^L \varphi^{IV}(x)\,\varphi(x)\,dx, \quad \theta_p=\vartheta_p\left(\frac{d\varphi(L)}{dx}-\frac{d\varphi(0)}{dx}\right),\\
& F_e=\frac{\varepsilon_0 a V_{DC}^2}{2}\int_0^L\left(\frac{H(x-d)}{(g_0-\bar{w})^2}-\frac{H(x-d)}{(g_0+\bar{w})^2}\right)\varphi(x)\,dx,\\
& F_b=z_0\Omega^2\int_0^L\Big((\rho A)_{eq}\varphi(x)+M_t\delta(x-L)\,\varphi(x)\Big)\,dx, \quad p_3=\frac{1}{2R}\\
& p_1=-\frac{\bar{e}_{31}a\,(h_0+h)}{2}\int_0^L \varphi^{II}(x)\,dx, \quad p_2=C_p.
\end{aligned}
\tag{24}
$$

By solving Eq. (22) and Eq. (23), the voltage across the resistance (v_p) and the dynamic deflection of the microbeam can be obtained. Therefore the harvested peak power from the piezoelectric layers can be expressed as

$$
P_p=\frac{\left|\{v_p\}_{\text{peak}}\right|^2}{R}. \tag{25}
$$

4 Numerical results and discussion

To demonstrate the analysis presented in Sect. 3, a clamped-free microbeam is considered with the characteristics introduced in Table 1. Shape functions, which satisfy the boundary conditions of the clamped–free micro-beam (with tip mass M_t), are considered of the form [31]

$$
\varphi_i(x)=A_r\left(\cos\lambda_i\frac{x}{L}-\cosh\lambda_i\frac{x}{L}+\varsigma_r\left(\sin\lambda_i\frac{x}{L}-\sinh\lambda_i\frac{x}{L}\right)\right), \tag{26}
$$

where

$$
\varsigma_r=\frac{\sin\lambda_i-\sinh\lambda_i+\lambda_i\frac{M_t}{(\rho A)_{eq}L}(\cos\lambda_i-\cosh\lambda_i)}{\cos\lambda_i+\cosh\lambda_i-\lambda_i\frac{M_t}{(\rho A)_{eq}L}(\sin\lambda_i-\sinh\lambda_i)},
$$

A_r is the modal amplitude constant and the eigenvalues of the system (λ_i for mode i) are obtained from

$$
\begin{aligned}
& 1+\cos\lambda_i\cosh\lambda_i+\lambda_i\frac{M_t}{(\rho A)_{eq}L}(\cos\lambda_i\sinh\lambda_i-\sin\lambda_i\cosh\lambda_i)\\
& -\frac{\lambda_i^3 I_t}{(\rho A)_{eq}L^3}(\cosh\lambda_i\sin\lambda_i+\sinh\lambda_i\cos\lambda_i)+\frac{\lambda_i^4 M_t I_t}{(\rho A)_{eq}L^3}(1-\cos\lambda_i\cosh\lambda_i)=0.
\end{aligned}
\tag{27}
$$

According to the solution of Eq. (16b), by increasing the applied voltages to the electrostatic areas, the electrical stiffness of the structure is increased and leads to the decrease of the equivalent stiffness of the structure. Therefore, at the pull-in voltage static instability occurs. Figure 4 shows the effect of the air gap between the electrodes on the pull-in voltage of the microbeam and the maximum amplitude of the electrostatic force (before the pull-in voltage) for $d=L/2$.

Table 1. Geometrical and material properties of the micro-beam and piezoelectric layers.

Design Variable	Value
Length of the beam (L)	$3000\,\mu$m
Width of the beam (a)	$1000\,\mu$m
Thickness of the beam (h)	$4\,\mu$m
Thickness of the piezoelectric layer (h_0)	$2\,\mu$m
Beam material Young's modulus (E)	169.6 GPa
Piezoelectric material Young's modulus (E_0)	65 GPa
Viscous air damping coefficient (c_a)	0.0002 N.s/m
Poisson's ratio (υ)	0.06
Beam material density (ρ)	$2330\,\mathrm{kg/m^3}$
Piezoelectric material density (ρ_0)	$7800\,\mathrm{kg/m^3}$
Equivalent piezoelectric coefficient ($\bar{e}_{31}$)	$-11.18\ \mathrm{Cm^{-2}}$
Permittivity component ($\bar{\varepsilon}_{33}^s$)	13.48 nF/m
Tip mass (M_t)	9.724×10^{-8} kg
Length of the tip mass (L_m)	$20\,\mu$m
Thickness of the tip mass (h_m)	$10\,\mu$m

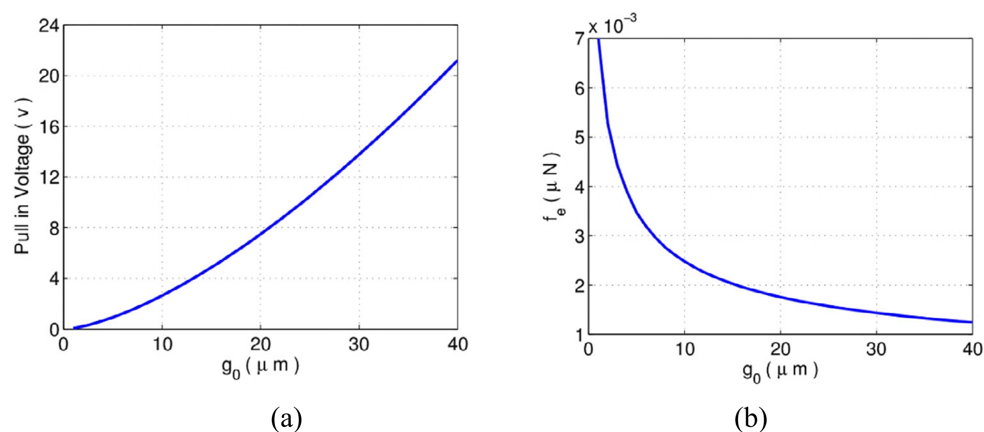

Fig. 4. Variation of the (a) pull in voltage and (b) the electrostatic force with the air gap between the electrodes (g_0).

Figure 4 shows that increasing the air gap between the electrodes decreases the electrostatic force (f_e) and increases the pull-in voltage. The natural frequency of the system also depends on the applied DC voltage and the air gap between the electrodes. Figure 5 illustrates the effects of these parameters on the open circuit natural frequency of the system. As shown in this figure, the natural frequency of the system is below 300 Hz which is suitable to harvest energy from ambient sources of vibration in nature. According to this figure, the natural frequency of the system decreases with increasing DC voltage and becomes zero at the pull-in voltage.

Based on the dynamic analysis of the system the harvested energy from the piezoelectric part of the harvester can be obtained from Eq. (25). There are some design considerations that can affect the harvested energy. Adjusting the natural frequency of the system to match the frequency of the base excitation will increase the output power of harvester. Choosing the optimal resistance is the second parameter which can increase the harvested power of the piezoelectric part. Figure 6 illustrates the optimal value of the resistance for different frequencies of base excitation when the

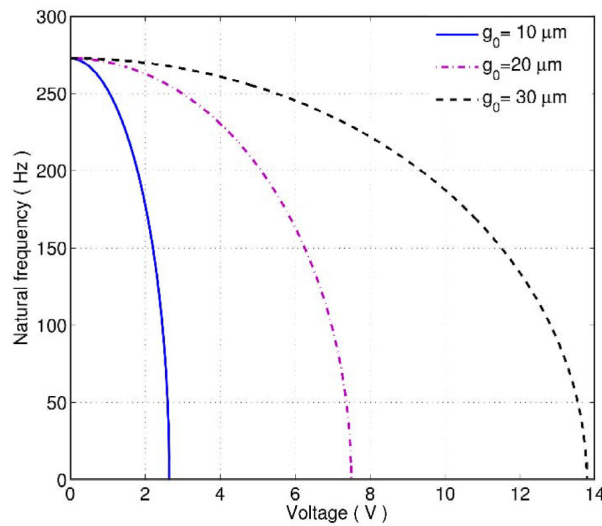

Fig. 5. Variation of the natural frequency with electrostatic voltage for different air gaps.

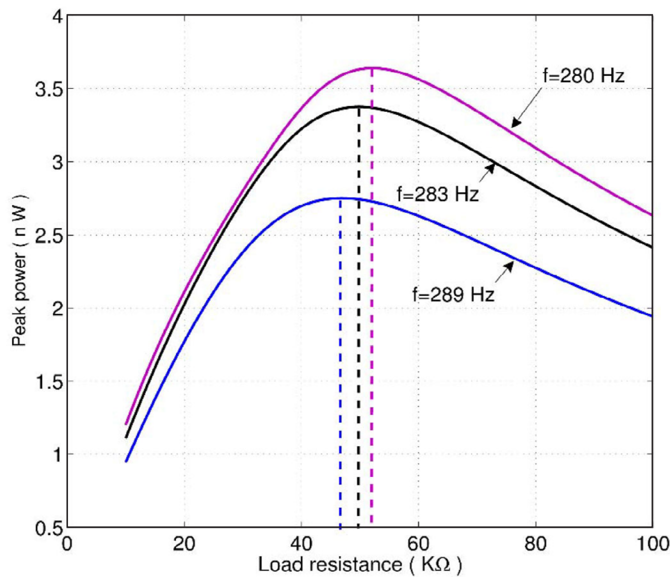

Fig. 6. Variation of the piezoelectric peak power with load resistance for different frequencies of base excitation.

amplitude of base excitation is $z_0 = 0.3\,\mu$m and 6 V is applied to the electrodes. The air gaps between the electrodes are equal with the value of $30\,\mu$m ($g_0 = 30\,\mu$m).

As seen in Fig. 6 the optimal value of the resistance reduces as the frequency of the base excitation increases. On the other hand, the electrostatic force can affect the performance of the piezoelectric part of the harvester. This effect mostly depends on the applied DC voltage and the air gap between the electrodes. Figures 7 and 8, shows the effect of the applied DC voltage and the air gap between electrodes on the performance of the system.

The applied DC voltage and the air gap between electrodes are able to adjust the resonance frequency of the system, to harvest the maximum power based on the

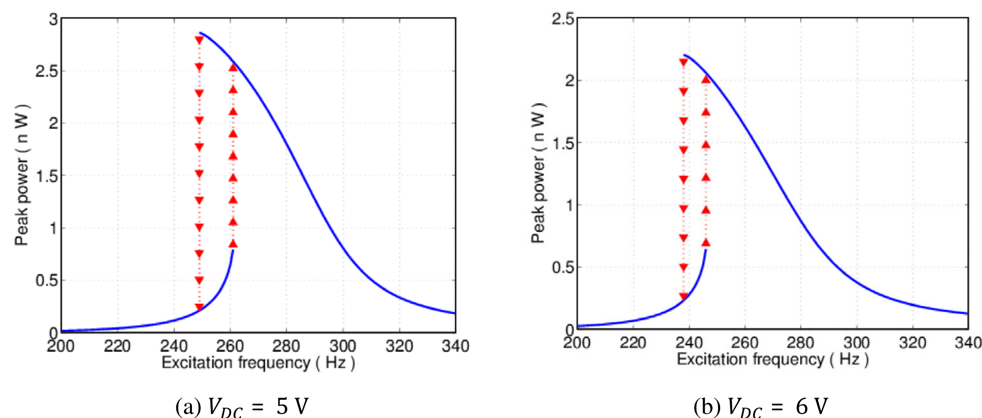

(a) V_{DC} = 5 V (b) V_{DC} = 6 V

Fig. 7. Variation of the piezoelectric peak power with the frequency of base excitation ($g_0 = 25\,\mu$m, $R = 80\,\mathrm{K}\Omega$).

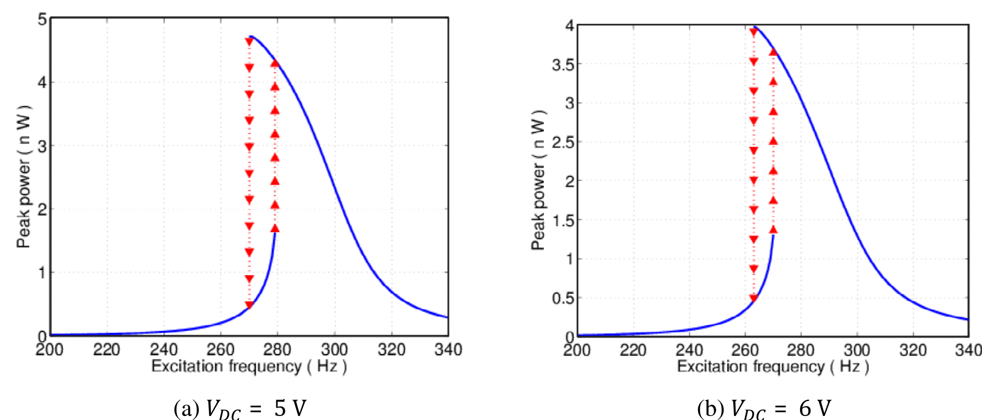

(a) V_{DC} = 5 V (b) V_{DC} = 6 V

Fig. 8. Variation of the piezoelectric peak power with the frequency of base excitation ($g_0 = 30\,\mu$m, $R = 80\,\mathrm{K}\Omega$).

frequency of the ambient source. In order to decrease the natural frequency of the system, either the applied DC voltage should be increased or the air gap between the electrodes should be reduced. On the other hand, decreasing the voltage and increasing the air gap can increase the natural frequency of the system. The initial gap between electrodes can be considered as a design parameter and is therefore fixed during operation. However, the applied DC voltage can vary and thus can be used to control the behaviour of the system via a variable voltage source. Figure 9 illustrates the possibility of changing dynamic behaviour of the system by applying the DC voltage at a constant air gap (assume $g_0 = 25\,\mu$m). Increasing the voltage from 4 V to 5 V reduces the resonance frequency of the system from 258 Hz to 249 Hz (see region R_1 in Fig. 9a), and from 5 V to 6 V reduces the resonance frequency from 249 Hz to 238 Hz (see region R_2 in Fig. 9b). This provides a wide range of resonance frequencies for the energy harvester system and hence the harvester system can be tuned by simply changing the applied voltage so that the system operates at its maximum efficiency.

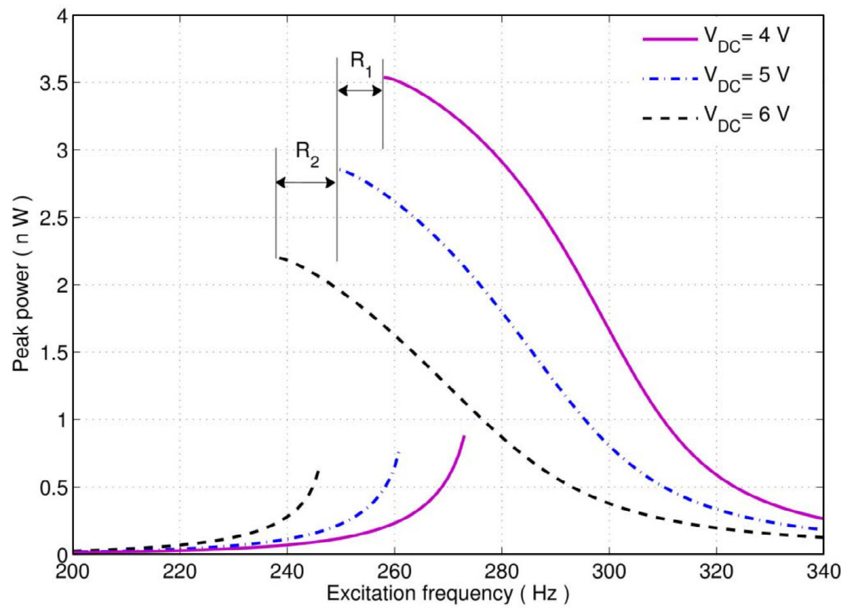

Fig. 9. Variation of the piezoelectric peak power with the frequency of base excitation ($g_0 = 25\,\mu\text{m}, R = 80\,\text{K}\Omega$).

By considering maximum peak power from each voltage, the optimal applied DC voltage can be found for different frequencies of ambient vibration sources. In order to avoid geometric and pull-in instability, the applied DC voltage has to be below the pull-in voltage and the maximum deflection of the beam has to be less than the air gap between the electrodes. Therefore, the air gap between electrodes has to be greater than the maximum deflection of the microbeam when the applied DC voltage equals zero. The downside of the proposed system is the softening nonlinear effect of the electrical stiffness; Fig. 9 shows that the maximum harvested power decreases as the voltage increases.

Figures 7, 8 and 9 show that there are multiple solutions for the beam response within the frequency range close to resonance, clearly identified as the excitation frequency is swept up and down. The response curves show the classical features of a softening nonlinear system with characteristic jumps at the ends of the regions of multiple solutions. For efficient energy harvesting the beam response should always occur at the higher of the two solutions and close to resonance (but not too close to risk jumping down to the low amplitude solution). However the solution actually obtained will depend on the initial conditions and hence the response at the high amplitude solution cannot be guaranteed. The control system using the applied DC voltage can be used to ensure the harvester always responds in the higher amplitude solution. For a given excitation frequency if the harvester response happens to be in the lower amplitude solution the DC voltage is increased until a region is reached where the harvester only has a single solution. The DC voltage is then slowly reduced and the harvester follows high amplitude solution until the resonance is obtained.

Based on the design considerations outlined previously the optimal applied DC voltage to harvest maximum power for a base excitation with amplitude $0.3\,\mu$m is shown in Fig. 10 for different frequencies of excitation. Without any DC voltage, significant power can be harvested only at the resonant frequency (see point A). However when the frequency of excitation is changed, the harvested power will be

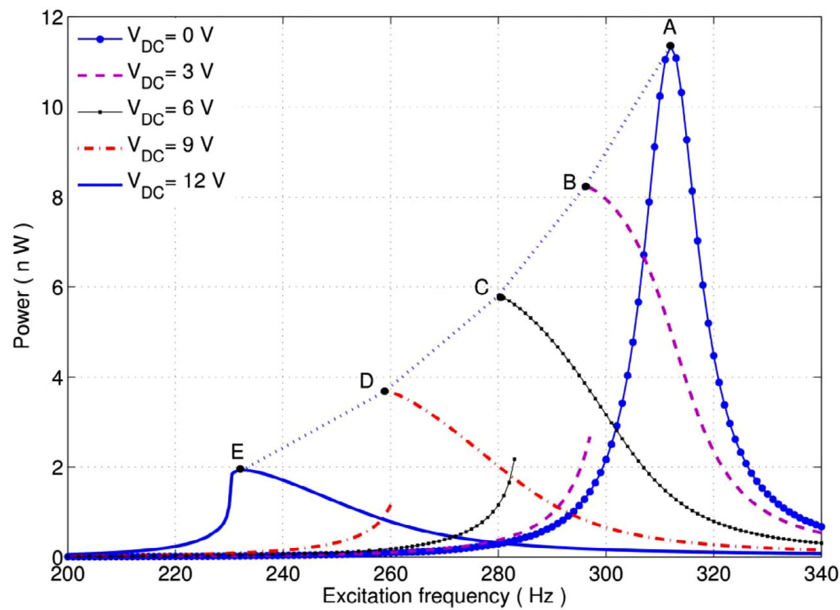

Fig. 10. Variation of the piezoelectric peak power with the frequency of base excitation ($g_0 = 35\,\mu\text{m}, R = 80\,\text{K}\Omega$).

reduced significantly. By increasing voltage from zero at point A to 12 V at point E we can find the optimal applied DC voltage for frequency range between 232 Hz to 312 Hz. Therefore, a variable voltage source can be used to increase the operational frequency band of the proposed harvester by simply matching the resonance frequency of the system to the frequency of the base excitation.

5 Conclusion

A hybrid piezoelectric electrostatic MEMS harvester which is capable of adjusting its resonance frequency to the excitation frequency is proposed in this paper. The main advantage of the proposed system is the use of an electrostatic device for the adaptive control of the natural frequency of the system. The numerical results showed that the natural frequency of the hybrid system is extremely sensitive to the applied DC voltage and therefore can be tuned by a variable voltage source in order to increase the operating frequency bandwidth of the harvester system. For a certain design, not necessarily the optimal design, it was shown the harvested system can cover a wide range of excitation frequencies, i.e. 232 Hz to 312 Hz. The disadvantage of the proposed system is the effect of the softening nonlinearity of the electrostatic part of the harvester which results in a lower level of harvested energy.

Hadi Madinei acknowledges the financial support from the Swansea University through the award of the Zienkiewicz scholarship.

References

1. M. Piotto, G. Pennelli, P. Bruschi, Microelectron. Eng. **88**, 2214 (2011)
2. S. Marauska, R. Jahns, C. Kirchhof, M. Claus, E. Quandt, R. Knöchel, B. Wagner, Sensors and Actuators A: Physical **89**, 321 (2013)

3. T. Galchev, H. Kim, K. Najafi, J. Microelectromech. Syst. **20**, 852 (2011)
4. S.P. Beeby, M.J. Tudor N.M. White, Meas. Sci. Technol. **17**, 175 (2006)
5. S. Roundy, P.K. Wright, J. Rabaey, Comp. Commun. **26**, 1131 (2003)
6. O. Zorlu, E.T. Topal, H. Kulah, IEEE Sensors J. **11**, 481 (2011)
7. T. Galchev, E.E. Aktakka, K. Najafi, IEEE J MEMS **21**, 1311 (2012)
8. D. Hoffmann, B. Folkmer, Y. Manoli, IOP J Micromech. Microeng. **19** (2009)
9. T.V. Buren, G. Troster, Sens. Actuators A, Phys. **135**, 765 (2007)
10. Y.B. Jeon, R. Sood, J.H. Jeong, S.G. Kim, Sensors and Actuators A: Physical **122**, 16 (2005)
11. W.J. Choi, Y. Jeon, J.H. Jeong, R. Sood, S.G. Kim, J. Electroceramics. **17**, 543 (2006)
12. H. Fang, J. Liu, Z. Zheng, L. Dong, D. Chen, B. Cai, Y. Liu, Chin. Phys. Lett. **23**, 732 (2006)
13. M. Renaud, T. Sterken, A. Schmitz, P.A.F.P. Fiorini, C.A.V.H.C. Van Hoof, R.A. Puers, in *Solid-State Sensors, Actuators and Microsystems Conference, Transducers International* (2007), p. 891
14. M. Renaud, K. Karakaya, T. Sterken, P. Fiorini, C. Van Hoof, R. Puers, Sensors and Actuators, A: Physical **145-146**, 380 (2008)
15. D. Shen, J. Park, J. Ajitsaria, S. Choe, H. Wikle, D. Kim, J. Micromech. Microeng. **18**, 055017 (2008)
16. L. Gu, Microelectron. J. **42**, 277 (2011)
17. L. Gu, C. Livermore, Smart Mater. Struct. **20**, 045004 (2011)
18. K. Vijayan, M.I. Friswell, H. Haddad Khodaparast, S. Adhikari, International J. Mechanical Sciences **96**, 101 (2015)
19. T.J. Kamierski, S. Beeby, *Energy Harvesting Systems Principles, Modeling and Applications*, 1st edn. (Springer, 2010)
20. J.S. Roundy, Ph.D. thesis, University of California at Berkeley, 2003
21. F. Peano, T. Tambosso, J. Microelectromechanical Systems **14**, 429 (2005)
22. B.C. Yen, J.H. Lang, IEEE Trans. Circuits Systems **53**, 288 (2006)
23. S. Meninger, J.O. Mur-Miranda, R. Amirtharajah, A.P. Chandrakasan, J.H. Lang, IEEE Trans. VLSI Syst. **9**, 64 (2001)
24. W. Ma, M. Wong, L. Ruber, in: *Proc. Design, Test, Integration and Packaging of MEMS and MOEMS* (2005), p. 380
25. I. Kuehne, A. Frey, D. Marinkovic, G. Eckstein, H. Seidel, Sens. Actuators **142**, 263 (2008)
26. Y. Chiu, V.F.G. Tseng, J. Micromech. Microeng. **18**, 104004 (2008)
27. P.D. Mitcheson, E.M. Yeatman, G.K. Rao, A.S. Holmes, T.C. Green, Proc. IEEE **96**, 1457 (2008)
28. T. Petropoulos, E.M. Yeatman, P.D. Mitcheson, MEMS coupled resonators for power generation and sensing, *Micromechanics Europe* (5–7 September 2004, Leuven, Belgium)
29. G.H. Feng, J.C. Hung, Optimal FOM designed piezoelectric microgenerator with energy harvesting in a wide vibration bandwidth, *Proc. 2nd IEEE Int. Conf. on. Nano/Micro Engineered and Molecular Systems* (16–19 January 2007, Bangkok, Thailand), p. 511
30. X. Wu, J. Lin, S. Kato, K. Zhang, T. Ren, L. Liu, A frequency adjustable vibration energy harvester, *Proc. Power MEMS 2008 + microEMS2008* (9–12 November 2008, Sendai, Japan), p. 245
31. A. Erturk, D.J. Inman, *Piezoelectric energy harvesting* (John Wiley & Sons, 2011)
32. H. Madinei, G. Rezazadeh, S. Azizi, J. Compu. Nonlinear Dyn. **10**, 021002 (2015)
33. H. Nayfeh, D.T. Mook, *Nonlinear Oscillations* (Wiley: New York, 1979)
34. H. Madinei, G. Rezazadeh, N. Sharafkhani, Microelectronics J. **44**, 1193 (2013)
35. G. Rezazadeh, M. Fathalilou, M. Sadeghi, Sens. Imaging J. **12**, 117 (2011)